Progress In Electromagnetics Research C, Vol. 166, 257–266, 2026

PIER C

(Received 10 November 2025, Accepted 30 December 2025, Scheduled 2 March 2026)

Fault-Tolerant Direct Torque Control with Harmonic Suppression for Dual Three-Phase SynRMs Using a Five-Leg Inverter

Ye Yuan[1], Yu Nan[1,*], Fan Yang[1], Yizhou Hua[2], Shusheng Li[3], Weiping Niu[1], Zhenzhen Kong[1], Xifeng Wang[1], and Sichao Chen[4]

[1]*Kaifeng Power Supply Company, State Grid Henan Electric Power Company, Kaifeng 475000, China*
[2]*School of Electrical and Information Engineering, Jiangsu University, Zhenjiang 212013, China*
[3]*Beijing Honghui International Energy Technology Development Co. Ltd., Beijing 100035, China*
[4]*Zhejiang Zhongxin Electric Power Engineering Construction Co., Ltd., Hangzhou 311215, China*

ABSTRACT: High reliability and stability are essential for drive systems in intelligent inspection robots used in the power industry. To meet this requirement, this study investigates dual three-phase synchronous reluctance motors and proposes a five-leg fault-tolerant drive strategy based on directtorque control (DTC). Unlike conventional dimension-reduction coordinate transformation methods that require isolating the faulty phase, which often leads to degraded system performance, the proposed approach introduces a bridge-arm sharing technique. By electrically coupling the faulty phase with a healthy phase, the spatial voltage vector distribution was reconstructed, enabling the reutilization of the faulty phase windings. Under single-phase fault conditions, the method effectively synthesizes the missing voltage vectors, preserves a circular flux linkage trajectory in the α-β subspace, suppresses the 5th and 7th harmonics, and improves the current waveform quality. Simulation results verify that the strategy delivers superior harmonic suppression, reduced torque ripple, and enhanced system reliability, offering a novel technical pathway for fault-tolerant control of multiphase motors with strong potential for engineering applications.

1. INTRODUCTION

With the rapid development of new-generation power systems, intelligent inspection robots have been widely deployed and become essential for maintaining stable grid operation [1]. The reliability of electricdrive systems is therefore of great importance, as failures in a drive stage may compromise inspection safety and operational efficiency [2]. In practice, inverter malfunctions as well as winding circuits and short-circuits occur frequently, posing risks to both the robot and power infrastructure [3]. Consequently, motor fault-tolerant control strategies capable of maintaining basic functionality under abnormal conditions are required, and such strategies are of significant theoretical and practical value [4].

Dual three-phase synchronous reluctance motors (SynRMs) have emerged as the preferred choice for high-reliability applications owing to their simple structure, high torque density, and low losses [5]. Compared to conventional three-phase machines, their inherent phase redundancy and abundant spatial voltage vector resources enable continued operation under single- or multi-phase faults through appropriate control strategies, thereby significantly enhancing fault tolerance and system reliability [6].

Field-oriented decoupling control combined with space vector modulation is widely adopted to enhance the steady-state performance of dual three-phase machines. However, as highlighted in studies examining the implementation of such control frameworks [7–9], multiple proportional-integral (PI) regulators are typically required to attenuate electromagnetic torque ripple and suppress harmonic currents. This reliance on numerous PI loops results in substantial parameter-tuning effort and necessitates real-time equation solving to compute the reference voltage vectors, thereby imposing a considerable computational burden. To address these limitations, direct torque control (DTC) was extended to multiphase permanent-magnet machines in [10–12]. Although DTC preserves its characteristic advantages of rapid torque response and strong robustness, these works also indicated that the inherent multidimensional subspace structure of multiphase machines was not fully utilized, leading to significant harmonic currents. Furthermore, [13, 14] introduced quasi-proportional-resonant (PR) regulators to achieve zero-steady-state-error tracking of specific harmonic current components, thereby mitigating current harmonics. Despite being effective in harmonic suppression, the incorporation of multiple resonant controllers inevitably increases the complexity of the overall control architecture. In [15, 16], a DTC scheme employing a T-type three-level inverter for dual three-phase permanent-magnet machines was proposed. These studies demonstrated that low-order harmonics can be effectively suppressed through harmonic closed-loop control; however, the increased number of phases inherently complicates both the system architecture and associated control algorithms.

* Corresponding author: Yu Nan (nanyu12024@163.com).

Although direct torque control strategies have been continuously refined, research efforts have also been extended to the field of fault-tolerant control to enhance machine reliability under fault conditions. In [17, 18], mathematical models of dual three-phase machines under different fault scenarios were established, and corresponding vector control and PWM strategies were proposed, laying the foundation for fault-tolerant operation under open-phase conditions. In [19], mathematical models for open-phase faults with various neutral-point connections were derived, and fault-tolerant current references were obtained by solving optimization problems constrained by minimizing stator copper loss. These approaches are primarily based on the principle of constant magnetomotive force (MMF). In [20], a conventional decoupling transformation matrix was employed, and two optimized current operation modes — minimum stator copper loss and maximum torque output — were analyzed. In [21, 22], the principle of instantaneous power invariance was adopted to realize fault-tolerant control schemes targeting stator copper loss minimization, thereby further improving machine performance under fault conditions.

In summary, although various conventional control methods and fault-tolerant strategies have been proposed for dual three-phase machines, several challenges remain. Harmonic suppression is often insufficient; control architectures are generally complex; and performance optimization under fault conditions is still limited. Therefore, a novel control strategy is required to simultaneously enhance harmonic suppression, simplify the overall architecture, and improve fault-tolerant performance.

To address these issues, a fault-tolerant control strategy for SynRMs based on a five-leg inverter topology was proposed. Bridge-arm sharing is employed so that the faulty-phase windings can still participate in the operation under open-phase conditions. In this way, fault-tolerant control is achieved, harmonic distortion effectively suppressed, and the overall system performance improved.

The main contributions of this paper are threefold:

1) A fault-tolerant control strategy was proposed for dual three-phase SynRMs using a five-leg inverter, enabling the continued operation of faulty-phase windings via bridge-arm sharing.

2) Voltage vector distribution and fault-tolerant synthesis were analyzed using a novel method that exploits extra degrees of freedom for efficient control in both healthy and faulty conditions.

3) The simulation results demonstrate superior flux trajectory preservation and reduced torque ripple, confirming the enhanced system performance over conventional approaches.

2. DIRECT TORQUE CONTROL WITH A HARMONIC SUPPRESSION SWITCHING TABLE

The electromechanical energy conversion of the dual three-phase SynRMs is confined to the α-β subspace [23]. Therefore, the DTC strategy can be derived from conventional three-phase machines. At the base speed and below, the torque and flux states are determined using hysteresis comparators. Combined with the sector number, the appropriate space voltage vector was selected from a predefined switching table. Thus, the control is performed in a two-phase stationary reference frame, eliminating the need for trigonometric calculations. Based on the mathematical model, the flux linkage, electromagnetic torque, and harmonic current equations can be formulated.

$$\begin{cases} \psi_{\mathrm{s}} = \int (U_{\mathrm{s}} - R_{\mathrm{s}} i_{\mathrm{s}}) dt \\ T_{\mathrm{e}} = 3p_n \left(i_\alpha \psi_\beta - i_\beta \psi_\alpha \right) = \frac{3p_n \psi_{\mathrm{s}}(t)}{L_{\mathrm{s}}} \sin \delta(t) \\ \begin{bmatrix} v_{z1} \\ v_{z2} \end{bmatrix} = R_s \begin{bmatrix} i_{z1} \\ i_{z2} \end{bmatrix} + \frac{d}{dt} \begin{bmatrix} i_{z1} \\ i_{z2} \end{bmatrix} \end{cases}, \tag{1}$$

The stator resistance R_s of the dual three-phase SynRMs is relatively small and can therefore be neglected. The variation rates of flux linkage and electromagnetic torque are obtained by differentiating and discretizing the first two equations in (1),

$$\begin{cases} \Delta \psi_{\mathrm{s}} = U_{\mathrm{s}} T_{\mathrm{s}} \\ \Delta T_{\mathrm{e}} = \frac{3p_n \psi_{\mathrm{s}} T_{\mathrm{s}} \cos \delta}{L_{\mathrm{s}}} \cdot \Delta \delta \end{cases}. \tag{2}$$

where T_s denotes the control period, and δ represents the torque angle.

From Eq. (2), the magnitude of the stator flux linkage $|\Psi_{\mathrm{s}}|$ can be approximated as the integral of the stator voltage over time. In practice, the control period T_{s} is extremely small. Consequently, the variation rate of $|\Psi_{\mathrm{s}}|$ is proportional to the projection of the applied voltage vector in the direction of Ψ_{s}. A longer projection led to a faster flux response. In DTC, $|\Psi_{\mathrm{s}}|$ is typically regulated to a constant reference value, whereas electromagnetic torque is determined by the angle δ between the stator and rotor flux linkages. The variation rate of the torque increased with the length of the voltage vector projection in the orthogonal direction, resulting in a faster torque response.

The DTC system of the dual three-phase SynRMs includes sector identification, flux estimation, torque calculation, and switching table design. The overall control block diagram is shown in Fig. 1.

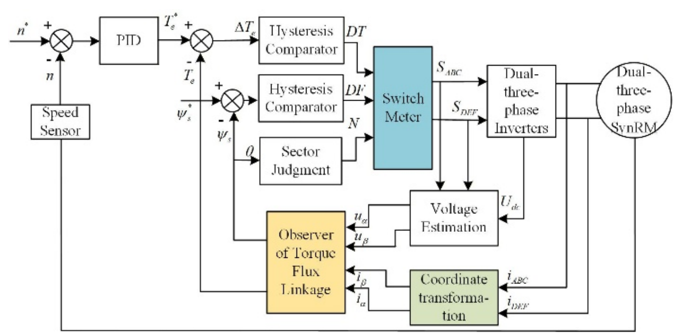

FIGURE 1. Direct torque control for the dual three-phase SynRMs.

To suppress low-order harmonics in the dual three-phase SynRMs and enhance the dynamic performance of the torque and flux linkage, 12 low-harmonic voltage vectors are employed to replace the original 12 large vectors [24]. A harmonic-suppression switching table was designed, as shown in Table 1. When selecting the control vectors, the criterion of

TABLE 1. Harmonic-suppression switching table.

		S_0	S_1	S_2	S_3	S_4	S_5
DF = 1	DT = 1	M_2	M_3	M_4	M_5	M_6	M_7
	DT = −1	M_{11}	M_{12}	M_1	M_2	M_3	M_4
DF = 0	DT = 1	M_5	M_6	M_7	M_8	M_9	M_{10}
	DT = −1	M_8	M_9	M_{10}	M_{11}	M_{12}	M_1
		S_6	S_7	S_8	S_9	S_{10}	S_{11}
DF = 1	DT = 1	M_8	M_9	M_{10}	M_{11}	M_{12}	M_1
	DT = −1	M_5	M_6	M_7	M_8	M_9	M_{10}
DF = 0	DT = 1	M_{11}	M_{12}	M_1	M_2	M_3	M_4
	DT = −1	M_2	M_3	M_4	M_5	M_6	M_7

achieving fast responses in both the torque and flux linkage is adopted instead of solely pursuing the fastest torque response, as in conventional DTC.

An example of sector S_0 is shown in Fig. 2. When both the torque and flux linkage must be increased (DT = DF = 1), three candidate vectors, M_1, M_2, M_3, can be selected. The analysis shows that M_1 provides the fastest flux response but the slowest torque response, whereas M_3 achieves the opposite. The response of M_2 lies between M_1 and M_3. In conventional DTC, M_3 is preferentially selected. However, because the synthesized vector of M_3 contains components that cannot simultaneously increase both torque and flux, M_2 is chosen as the control vector instead. Vector M_2 is synthesized from V_9, V_{11}, and V_{27}, enabling the simultaneous enhancement of torque and flux while achieving high utilization of the space voltage vectors.

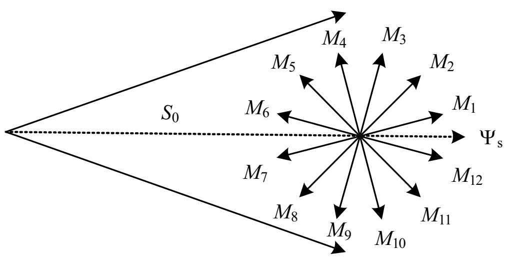

FIGURE 2. Analysis of low-harmonic vector control performance.

The control effects of the voltage vectors under different operating conditions across 12 sectors were analyzed. Finally, a harmonic-suppression switching table is obtained. This method preserves the advantages of conventional DTC, such as a low computational burden and simple implementation, while effectively reducing the system switching frequency and maintaining symmetric output waveforms.

3. ARCHITECTURE AND PRINCIPLES OF FAULT-TOLERANT DRIVE SYSTEMS

Faults such as short circuits and open circuits in the dual three-phase SynRMs can be isolated through the PWM control of the corresponding single-phase inverter. As a result, these faults can be uniformly transformed into open-phase faults [25], and fault-tolerant control is therefore mainly focused on the inverter open-phase conditions. Because the characteristics of open-phase faults are similar across all phases, the case of an open fault in phase F was considered as an example in this study. The main circuit configuration for the single-phase open-circuit fault is shown in Fig. 3.

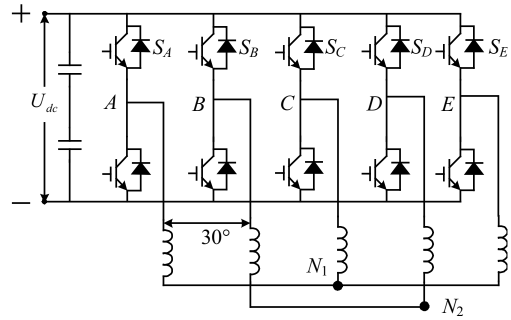

FIGURE 3. Main circuit configuration of the dual three-phase SynRMs under an open-circuit fault in phase F.

When an open-circuit fault occurs in phase F, the relationship between the phase voltages of the remaining five phases and their corresponding voltages is given by:

$$\left\{\begin{array}{l} u_{\mathrm{A}} = u_{\mathrm{AO}} - u_{\mathrm{N1O}} = (2S_{\mathrm{A}} - 1)\,\frac{U_{\mathrm{dc}}}{2} - u_{\mathrm{N1O}} \\ u_{\mathrm{B}} = u_{\mathrm{BO}} - u_{\mathrm{N1O}} = (2S_{\mathrm{B}} - 1)\,\frac{U_{\mathrm{dc}}}{2} - u_{\mathrm{N1O}} \\ u_{\mathrm{C}} = u_{\mathrm{CO}} - u_{\mathrm{N1O}} = (2S_{\mathrm{C}} - 1)\,\frac{U_{\mathrm{dc}}}{2} - u_{\mathrm{N1O}} \\ u_{\mathrm{D}} = u_{\mathrm{DO}} - u_{\mathrm{N2O}} = (2S_{\mathrm{D}} - 1)\,\frac{U_{\mathrm{dc}}}{2} - u_{\mathrm{N2O}} \\ u_{\mathrm{E}} = u_{\mathrm{EO}} - u_{\mathrm{N2O}} = (2S_{\mathrm{E}} - 1)\,\frac{U_{\mathrm{dc}}}{2} - u_{\mathrm{N2O}} \end{array}\right. . \tag{3}$$

where u_{A}, u_{B}, u_{C}, u_{D}, and u_{E} denote the phase voltages of the five remaining phases; S_{A}, S_{B}, S_{C}, S_{D}, and S_{E} represent the switching states of each phase's bridge arms, where a value of 1 indicates that the upper switch is ON, and the lower switch is OFF, while a value of 0 indicates the opposite state; U_{N1O} and u_{N2O} denote the neutral-point voltages of the dual three-phase SynRMs with respect to the midpoint of the DC bus.

4. FAULT-TOLERANT CONTROL OF DUAL THREE-PHASE SYNRMS WITH A FIVE-LEG INVERTER

4.1. Principle of Five-Leg-Inverter-Based Fault-Tolerant Control

Although traditional dimension-reduction fault-tolerant methods are feasible, the faulty-phase windings must be isolated and discarded, which leads to a complicated implementation process. To simplify the fault-tolerant control of dual three-phase machines, a five-leg inverter driving strategy is investigated, which enables continued utilization of the faulty-phase windings, thereby simplifying the control structure and improving system performance.

As shown in Fig. 4, after an open-circuit fault occurs in phase F, only 32 voltage vectors remain available in both the α-β and Z_1-Z_2 subspaces. Among the twelve large vectors on the periphery of the α-β subspace, only six are retained; multiple vectors in the lower sectors become unavailable, resulting in the inability to synthesize certain sector vectors. When a non-faulty phase is used for compensation, such as sharing the bridge arm

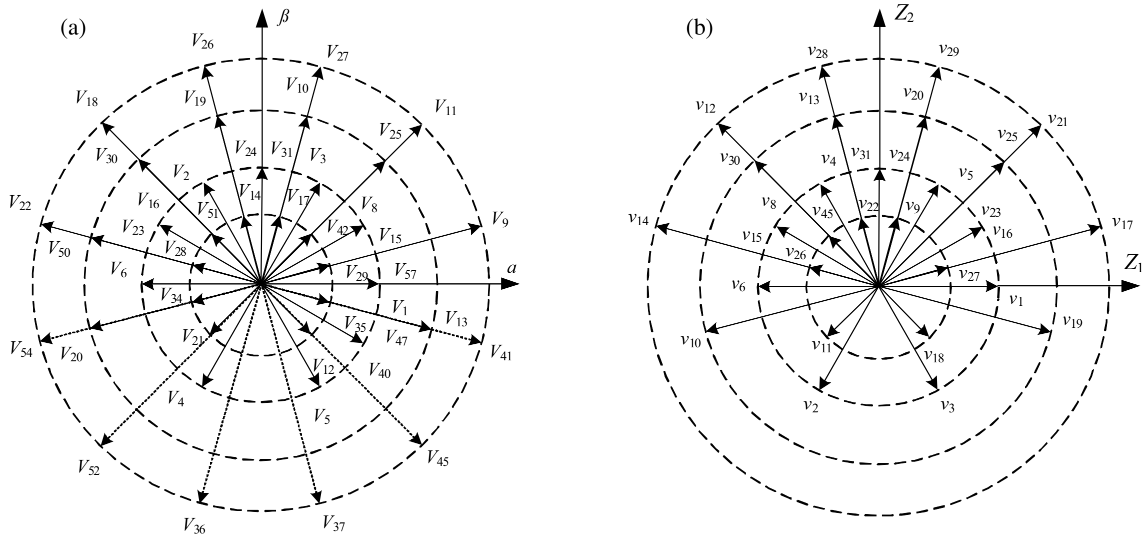

FIGURE 4. Space voltage vector distribution after an F-phase open-circuit fault. (a) Voltage vector distribution in the α-β subspace. (b) Voltage vector distribution in the Z_1-Z_2 subspace.

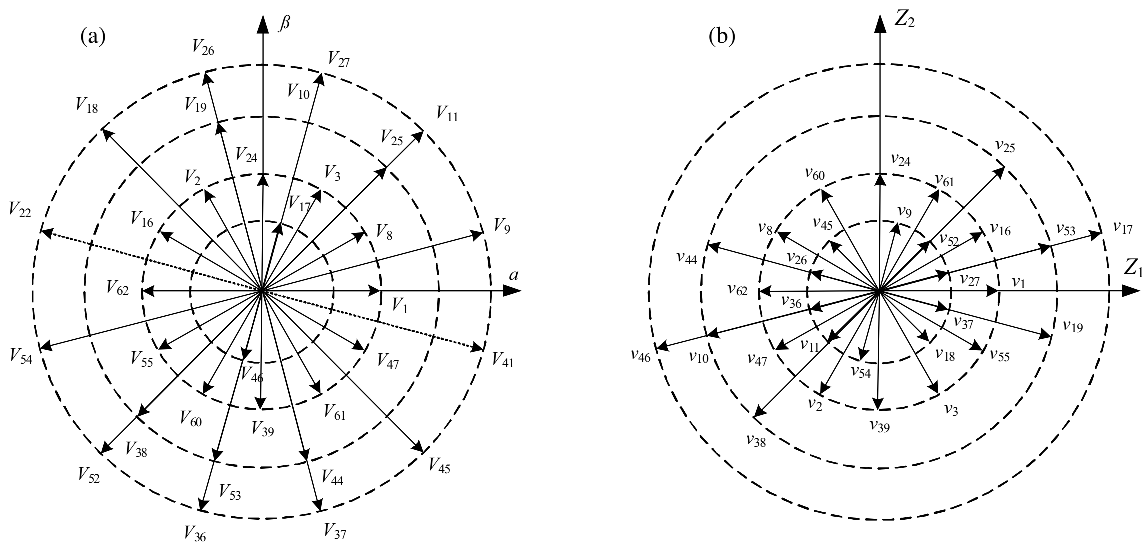

FIGURE 5. Voltage vector distribution after phase C shares the bridge arm with phase F. (a) Voltage vector distribution in the α-β subspace. (b) Voltage vector distribution in the Z_1-Z_2 subspace.

of phase C to compensate for phase F, the distribution of space voltage vectors in both the α-β and Z_1-Z_2 subspaces is illustrated in Fig. 5.

As shown in Fig. 5, after phases C and F share the bridge arm, thirty-two voltage vectors remain available in both the α-β and Z_1-Z_2 subspaces. The distribution becomes more uniform, and no large continuous sector is missing. Among the twelve large vectors on the periphery of the α-β subspace, ten are retained, and the missing ones are compensated by basic vectors, which facilitates fault-tolerant vector synthesis.

4.2. Fault-Tolerant Vector Synthesis Method

In Fig. 5, ten out of the 12 large vectors on the periphery of the α-β subspace remain available. The low-harmonic vectors M_2, M_3, M_4, M_8, M_9, and M_{10} can still be synthesized from three adjacent large vectors and directly applied. However, M_1, M_5, M_6, M_7, M_{11}, and M_{12} require a new synthesis method. Among them, M_1, M_5, M_7, and M_{11} belong to the first category, while M_6 and M_{12} belong to the second category.

In the first category, the five-leg fault-tolerant vector at the position of M_1 is denoted as V_1^{**}, which is synthesized from V_1, V_9, V_{11}, and V_{47}. Its magnitude $|V_1^{**}|$ and the corresponding application times T_1, T_2, T_3, and T_4 are calculated. As shown in Fig. 6, the target vector is located at the position of V_9 in the α-β subspace, and (4) and (5) can be obtained accordingly.

$$|V_1^{**}|T_s = |V_1|T_1\cos(15^\circ) + |V_9|T_2 + |V_{11}|T_3\cos(30^\circ) + |V_{47}|T_4\cos(45^\circ), \tag{4}$$

$$|V_1|T_1\sin(15^\circ) + |V_{47}|T_4\sin(45^\circ) = |V_{11}|T_3\sin(30^\circ). \tag{5}$$

where $|V_9| = |V_{11}| = |v_{\max}| \approx 0.644U_{dc}$, $|V_1| = |V_{47}| = |v_{bas}| \approx 0.333U_{dc}$.

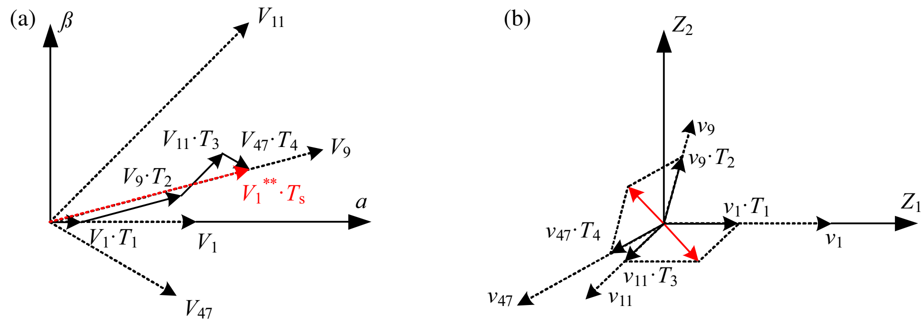

FIGURE 6. Illustration of the synthesis process for the first-category fault-tolerant vectors. (a) Synthesized fault-tolerant vector V_1^{**} in the α-β subspace. (b) Mutual cancellation in the Z_1-Z_2 subspace.

In the Z_1-Z_2 subspace, the mappings of vectors V_1, V_9, V_{11}, and V_{47}, denoted as v_1, v_9, v_{11}, and v_{47}, are required to cancel each other. Eqs. (6) and (7) are thus obtained.

$$\begin{aligned}&|v_1|\,T_1\cos(30^\circ)+|v_9|\,T_2\cos(45^\circ)\\&=|v_{11}|\,T_3\cos(15^\circ)+|v_{47}|\,T_4,\end{aligned}\tag{6}$$

$$|v_1|\,T_1\sin(30^\circ)+|v_{11}|\,T_3\sin(15^\circ)=|v_9|\,T_2\sin(45^\circ).\tag{7}$$

where $|v_9|=|v_{11}|=|v_{\min}|\approx 0.173U_{\mathrm{dc}}$, $|v_1|=|v_{47}|=|v_{\mathrm{bas}}|\approx 0.333U_{\mathrm{dc}}$.

The total application time of the four synthesized vectors is required to satisfy:

$$T_s=T_1+T_2+T_3+T_4,\tag{8}$$

The simultaneous solution of (4)–(8) yields:

$$\begin{cases}|V_1^{**}|=\frac{\sqrt{2}}{3}U_{dc}\approx 0.4714U_{dc}\\ T_1=T_3=T_4=\frac{3-\sqrt{3}}{6}T_s\approx 0.2113T_s\\ T_2=\frac{\sqrt{3}-1}{2}T_s\approx 0.3661T_s\end{cases},\tag{9}$$

The synthesized five-leg fault-tolerant vector has a magnitude of $|V_1^{**}|=0.4714U_{\mathrm{dc}}$. Within one control period T_{s}, the application times of the composing vectors V_1, V_9, V_{11}, and V_{47} are approximately $0.2113T_{\mathrm{s}}$, $0.4893T_{\mathrm{s}}$, $0.2113T_{\mathrm{s}}$, and $0.2113T_{\mathrm{s}}$, respectively. Based on these values, the phase PWM waveforms are plotted as shown in Fig. 7.

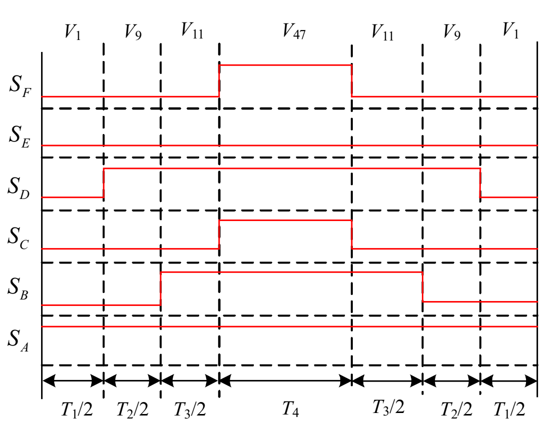

FIGURE 7. Phase PWM waveforms corresponding to the fault-tolerant control vector V_1^{**}.

For the second category, taking the vector at the M_{12} position as an example, the fault-tolerant vector V_{12}^{**} is synthesized from V_1, V_9, V_{45}, and V_{47}. Its magnitude $|V_{12}^{**}|$ and the application times T_1, T_2, T_3, and T_4 of the composing vectors within one control period T_s are calculated. As shown in Fig. 8, the target vector is located at the position of V_{41} in the α-β subspace, and (10) and (11) are thus obtained.

$$\begin{aligned}|V_{12}^{**}|\,T_s=&|V_1|\,T_1\cos(15^\circ)+|V_9|\,T_2\cos(30^\circ)\\&+|V_{45}|\,T_3\cos(30^\circ)+|V_{47}|\,T_4\cos(15^\circ),\end{aligned}\tag{10}$$

$$\begin{aligned}&|V_1|\,T_1\sin(15^\circ)+|V_9|\,T_2\sin(30^\circ)\\&=|V_{45}|\,T_3\sin(30^\circ)+|V_{47}|\,T_4\sin(15^\circ).\end{aligned}\tag{11}$$

where $|V_9|=|V_{45}|=|v_{\max}|\approx 0.644U_{\mathrm{dc}}$; $|V_1|=|V_{47}|=|v_{\mathrm{bas}}|\approx 0.333U_{\mathrm{dc}}$.

In the Z_1-Z_2 subspace, the mappings of vectors V_1, V_9, V_{45}, and V_{47}, denoted as v_1, v_9, v_{45}, and v_{47}, are required to cancel each other. Eqs. (12) and (13) are thus obtained.

$$\begin{aligned}&|v_1|\,T_1\cos(75^\circ)+|v_{47}|\,T_4\cos(75^\circ)\\=\;&|v_9|\,T_2\cos(30^\circ)=|v_{45}|\,T_3\cos(30^\circ),\end{aligned}\tag{12}$$

$$\begin{aligned}&|v_1|\,T_1\sin(75^\circ)+|v_9|\,T_3\sin(30^\circ)\\=\;&|v_{45}|\,T_3\sin(30^\circ)+|v_{47}|\,T_4\sin(75^\circ).\end{aligned}\tag{13}$$

where $|v_9|=|v_{45}|=|v_{\min}|\approx 0.173U_{\mathrm{dc}}$; $|v_1|=|v_{47}|=|v_{\mathrm{bas}}|\approx 0.333U_{\mathrm{dc}}$.

The total application time of the four synthesized vectors is required to satisfy:

$$T_s=T_1+T_2+T_3+T_4.\tag{14}$$

The simultaneous solution of (10)–(14) yields:

$$\begin{cases}|V_{12}^{**}|=\frac{\sqrt{6}}{6}U_{dc}\approx 0.4082U_{dc}\\ T_1=T_4=\frac{3-\sqrt{3}}{4}T_s\approx 0.317T_s\\ T_2=T_3=\frac{\sqrt{3}-1}{4}T_s\approx 0.183T_s\end{cases}.\tag{15}$$

The synthesized five-leg fault-tolerant vector has a magnitude of $|V_{12}^{**}|=0.4082U_{\mathrm{dc}}$. Within one control period T_{s}, the application times of the composing vectors V_1, V_9, V_{45}, and V_{47} are approximately $0.317T_{\mathrm{s}}$, $0.183T_{\mathrm{s}}$, $0.183T_{\mathrm{s}}$, and $0.317T_{\mathrm{s}}$, respectively; based on these values, the phase PWM waveforms are plotted as shown in Fig. 9.

The synthesis methods of the two fault-tolerant vectors, V_1^{**} and V_{12}^{**}, are representative of all six fault-tolerant control vec-

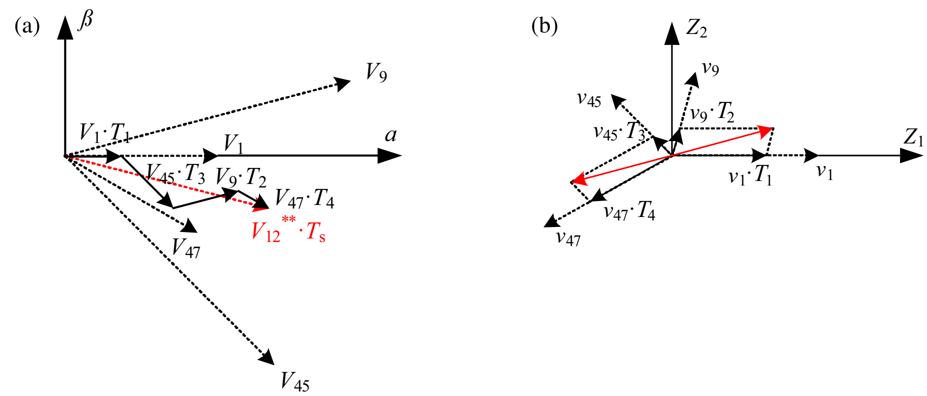

FIGURE 8. Illustration of the synthesis process for the second-category fault-tolerant vectors. (a) Synthesized fault-tolerant vector V_{12}^{**} in the α-β subspace. (b) Mutual cancellation in the Z_1-Z_2 subspace.

TABLE 2. Synthesis of fault-tolerant vectors for the five-leg dual three-phase drive.

Original vector	Synthesis vectors and Invocation time				Fault-Tolerant Vector for Five-Leg Inverter	Vector Magnitude
V_9	V_1 $0.2113T_s$	V_9 $0.3661T_s$	V_{11} $0.2113T_s$	V_{47} $0.2113T_s$	V_1^{**}	$0.4714U_{\rm dc}$
V_{11}	V_{27} $0.2679T_s$	V_{11} $0.4642T_s$	V_9 $0.2679T_s$	× ×	V_2^{**}	$0.5977U_{\rm dc}$
V_{27}	V_{26} $0.2679T_s$	V_{27} $0.4642T_s$	V_{11} $0.2679T_s$	× ×	V_3^{**}	$0.5977U_{\rm dc}$
V_{26}	V_{18} $0.2679T_s$	V_{26} $0.4642T_s$	V_{27} $0.2679T_s$	× ×	V_4^{**}	$0.5977U_{\rm dc}$
V_{18}	V_{16} $0.2113T_s$	V_{18} $0.3661T_s$	V_{26} $0.2113T_s$	V_{62} $0.2113T_s$	V_5^{**}	$0.4714U_{\rm dc}$
V_{22}	V_{16} $0.317T_s$	V_{18} $0.183T_s$	V_{62} $0.183T_s$	V_{54} $0.317T_s$	V_6^{**}	$0.4082U_{\rm dc}$
V_{54}	V_{16} $0.2113T_s$	V_{52} $0.3661T_s$	V_{54} $0.2113T_s$	V_{62} $0.2113T_s$	V_7^{**}	$0.4714U_{\rm dc}$
V_{52}	V_{36} $0.2679T_s$	V_{52} $0.4642T_s$	V_{54} $0.2679T_s$	× ×	V_8^{**}	$0.5977U_{\rm dc}$
V_{36}	V_{37} $0.2679T_s$	V_{36} $0.4642T_s$	V_{52} $0.2679T_s$	× ×	V_9^{**}	$0.5977U_{\rm dc}$
V_{37}	V_{45} $0.2679T_s$	V_{37} $0.4642T_s$	V_{36} $0.2679T_s$	× ×	V_{10}^{**}	$0.5977U_{\rm dc}$
V_{45}	V_1 $0.2113T_s$	V_{37} $0.3661T_s$	V_{45} $0.2113T_s$	V_{47} $0.2113T_s$	V_{11}^{**}	$0.4714U_{\rm dc}$
V_{41}	V_1 $0.317T_s$	V_9 $0.183T_s$	V_{45} $0.183T_s$	V_{47} $0.317T_s$	V_{12}^{**}	$0.4082U_{\rm dc}$

tors that require resynthesis. The synthesis of the remaining six fault-tolerant vectors is identical to that of the low-harmonic vectors, and after completing all calculations, the synthesis table for the five-leg fault-tolerant vectors of the dual three-phase drive is obtained, as presented in Table 2.

4.3. Design of Switching Table for Fault-Tolerant Operation

The twelve fault-tolerant control vectors of the five-leg drive have three distinct magnitudes: $0.5977U_{\rm dc}$, $0.4714U_{\rm dc}$, and $0.4082U_{\rm dc}$.

Their positions are identical to those of the low-harmonic vectors, and the control performance for torque and flux linkage remains unchanged. By mapping them to the corresponding low-harmonic vectors, the fault-tolerant switching table shown in Table 3 is obtained.

4.4. Analysis of DC-Bus Voltage Utilization

The modulation index is the ratio of the fundamental phase voltage amplitude to the DC bus voltage, facilitating the analysis of

TABLE 3. Fault-tolerant switching table for the five-leg dual three-phase drive.

		S_0	S_1	S_2	S_3	S_4	S_5
DF = 1	DT = 1	V_2^{**}	V_3^{**}	V_4^{**}	V_5^{**}	V_6^{**}	V_7^{**}
	DT = −1	V_{11}^{**}	V_{12}^{**}	V_1^{**}	V_2^{**}	V_3^{**}	V_4^{**}
DF = 0	DT = 1	V_5^{**}	V_6^{**}	V_7^{**}	V_8^{**}	V_9^{**}	V_{10}^{**}
	DT = −1	V_8^{**}	V_9^{**}	V_{10}^{**}	V_{11}^{**}	V_{12}^{**}	V_1^{**}
		S_6	S_7	S_8	S_9	S_{10}	S_{11}
DF = 1	DT = 1	V_8^{**}	V_9^{**}	V_{10}^{**}	V_{11}^{**}	V_{12}^{**}	V_1^{**}
	DT = −1	V_5^{**}	V_6^{**}	V_7^{**}	V_8^{**}	V_9^{**}	V_{10}^{**}
DF = 0	DT = 1	V_{11}^{**}	V_{12}^{**}	V_1^{**}	V_2^{**}	V_3^{**}	V_4^{**}
	DT = −1	V_2^{**}	V_3^{**}	V_4^{**}	V_5^{**}	V_6^{**}	V_7^{**}

the DC bus voltage utilization.

$$m = |V| / U_{dc}. \tag{16}$$

The reference voltages of each phase in the dual three-phase SynRMs are given by:

$$\begin{cases} u_{\mathrm{A}} = mU_{\mathrm{dc}} \cos\theta \\ u_{\mathrm{B}} = mU_{\mathrm{dc}} \cos(\theta - 2\pi/3) \\ u_{\mathrm{C}} = mU_{\mathrm{dc}} \cos(\theta + 2\pi/3) \\ u_{\mathrm{D}} = mU_{\mathrm{dc}} \cos(\theta - \pi/6) \\ u_{\mathrm{E}} = mU_{\mathrm{dc}} \cos(\theta - 5\pi/6) \\ u_{\mathrm{F}} = mU_{\mathrm{dc}} \cos(\theta + \pi/2) \end{cases}. \tag{17}$$

In the dual three-phase SynRMs considered in this study, the neutral points of the two sets of windings were isolated. Therefore, only the line-to-line voltages of a three-phase winding must be calculated. Using u_{AC} as an example:

$$\begin{aligned} u_{\mathrm{AC}} &= mU_{\mathrm{dc}} \cos\theta - mU_{\mathrm{dc}} \cos(\theta - 2\pi/3) \\ &= -\sqrt{3} mU_{\mathrm{dc}} \sin(\theta - \pi/3). \end{aligned} \tag{18}$$

In practice, the amplitude of the motor line-to-line voltage is always smaller than the DC bus voltage.

$$|u_{\mathrm{AC}}| \leq \sqrt{3} mU_{\mathrm{dc}} \leq U_{\mathrm{dc}}. \tag{19}$$

By substituting (18) into (19), the linear maximum modulation index under the normal operation of the dual three-phase SynRMs is obtained as $0.577U_{\mathrm{dc}}$. Under a single-phase fault (e.g., phase F), a five-leg fault-tolerant strategy was adopted, with phases C and F sharing one bridge arm. The two three-phase windings became asymmetrical and coupled, whereas the modulation index remained unchanged. The line-to-line voltage u_{AD} is then given by:

$$\begin{aligned} u_{\mathrm{AD}} &= u_{\mathrm{AC}} + u_{\mathrm{FD}} = mU_{\mathrm{dc}} \cos\theta - mU_{\mathrm{dc}} \cos(\theta + 2\pi/3) \\ &\quad + mU_{\mathrm{dc}} \cos(\theta + \pi/2) - mU_{\mathrm{dc}} \cos(\theta - \pi/6) \\ &= 2\sqrt{3} \sin(\pi/12) mU_{\mathrm{dc}} \cos(\theta + \pi/4). \end{aligned} \tag{20}$$

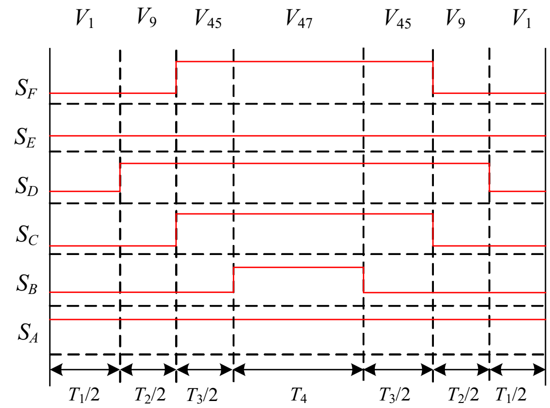

FIGURE 9. Phase PWM waveforms corresponding to fault-tolerant control vector V_{12}^{**}.

The expressions for the line-to-line voltages u_{AE}, u_{BD}, and u_{BE} are given by:

$$\begin{aligned} u_{\mathrm{AE}} &= u_{\mathrm{AC}} + u_{\mathrm{FE}} = \sqrt{6} mU_{\mathrm{dc}} \cos(\theta + \pi/12) \\ u_{\mathrm{BD}} &= u_{\mathrm{BC}} + u_{\mathrm{FD}} \\ &\quad = -2\sqrt{3} \sin(\pi/12) mU_{\mathrm{dc}} \cos(\theta + \pi/12) \\ u_{\mathrm{BE}} &= u_{\mathrm{BC}} + u_{\mathrm{FE}} \\ &\quad = 2\sqrt{3} \sin(\pi/12) mU_{\mathrm{dc}} \cos(\theta - \pi/12) u_{\mathrm{AE}} \, |u_{\mathrm{AE}}| \\ &\quad \leq \sqrt{6} mU_{\mathrm{dc}} \leq U_{\mathrm{dc}}. \end{aligned} \tag{21}$$

where the line-to-line voltage with the maximum amplitude is u_{AE}, and its magnitude must satisfy:

$$|u_{\mathrm{AE}}| \leq \sqrt{6} mU_{\mathrm{dc}} \leq U_{\mathrm{dc}}. \tag{22}$$

It is obtained that $m \leq 1/\sqrt{6} \approx 0.408$. Therefore, under the C-phase and F-phase bridge-sharing fault-tolerant operation mode, the maximum linear modulation index of the system is $0.408U_{\mathrm{dc}}$, which is approximately 70.71% of that under normal operation.

4.5. Applicability of the Proposed Strategy to Other Single-Phase Open-Circuit Faults

Although the analysis in this paper focuses on an open-circuit fault in phase F, the proposed five-leg fault-tolerant strategy was fully applicable to open-circuit faults occurring in any of the six phases. This generalizability arises from the inherent 60° electrical symmetry of the dual three-phase winding structure. When a different phase experiences an open-circuit fault, the resulting loss of available voltage vectors in both the α-β and Z_1-Z_2 subspaces is identical to the F-phase case, except for a uniform rotational shift.

Accordingly, the bridge-arm sharing scheme can be directly extended by rotating the healthy phase and faulty phase pairing according to the phase sequence. The geometric relationships among voltage vectors remain unchanged under such rotation, meaning that the synthesis principles and switching-time calculations (T_1-T_4) derived in Sections 4.2 and 4.3 remain valid

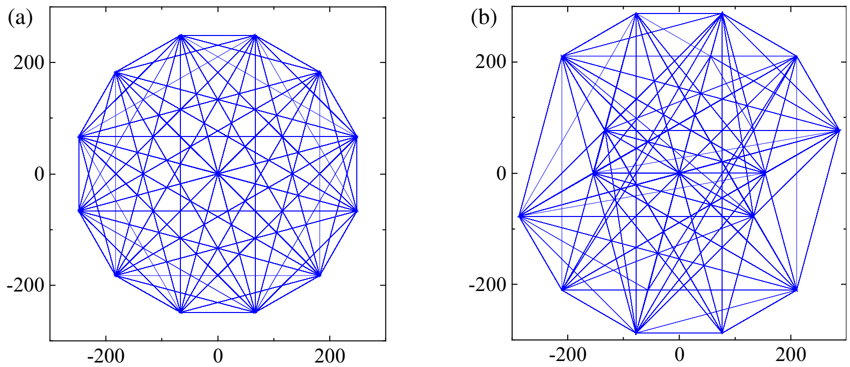

FIGURE 10. Comparison of space voltage vector trajectories. (a) Normal operation. (b) Five-leg drive under fault-tolerant operation.

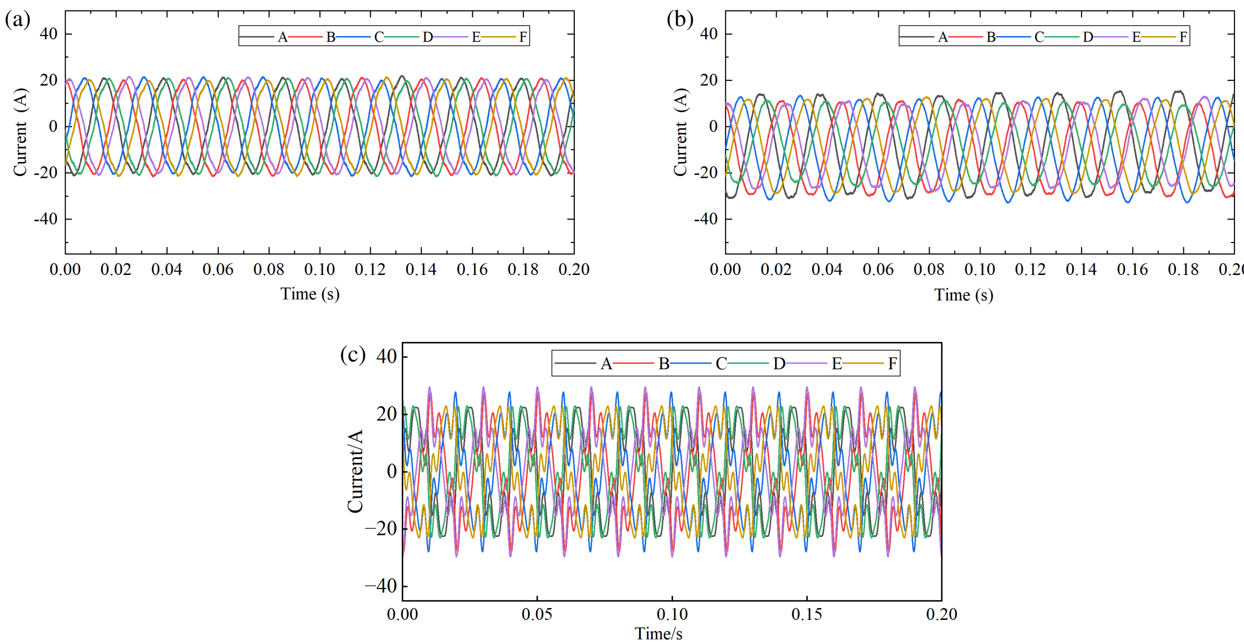

FIGURE 11. Comparison of phase currents. (a) Normal operation. (b) The fault-tolerant operation.

without modification. Only the corresponding vector indices require cyclic reassignment.

Similarly, the fault-tolerant switching table can be obtained by applying a sector-wise circular mapping, ensuring that the DTC decision logic remains consistent across all single-phase fault scenarios. Therefore, the proposed method maintains its effectiveness and structural simplicity regardless of which phase encounters an open-circuit fault, demonstrating strong generalizability and practical applicability.

5. VERIFICATION OF THE FAULT-TOLERANT STRATEGY

To validate the proposed fault-tolerant control strategy, a simulation model of the five-leg dual three-phase SynRM drive was established in Simulink.

As illustrated in Fig. 10, after a fault occurs in phase F, the outermost large voltage vectors V_{22} and V_{41} are no longer available. Nevertheless, the remaining vector set still enables an effective voltage synthesis through appropriate modulation. This confirms that despite partial vector loss, the proposed fault-tolerant control strategy can reconstruct the required reference voltage by utilizing the inner and intermediate vectors. The continuity of vector synthesis ensures stable operation and supports the theoretical analysis of vector space reconfiguration under fault conditions.

As illustrated in Fig. 11, when phase F is subjected to a fault, the dual three-phase synchronous reluctance motors are reconfigured by connecting phase F to phase C, while all phase windings remain energized. In this manner, the original dual three-phase structures are essentially preserved. Before and after the fault, the phase currents are maintained in nearly sinusoidal form. Under sufficient switching device margins, the overall motor performance is scarcely affected. By comparing Fig. 10(a) and Fig. 10(b), it can be observed that although slight distortions occur in certain phase currents, the si-

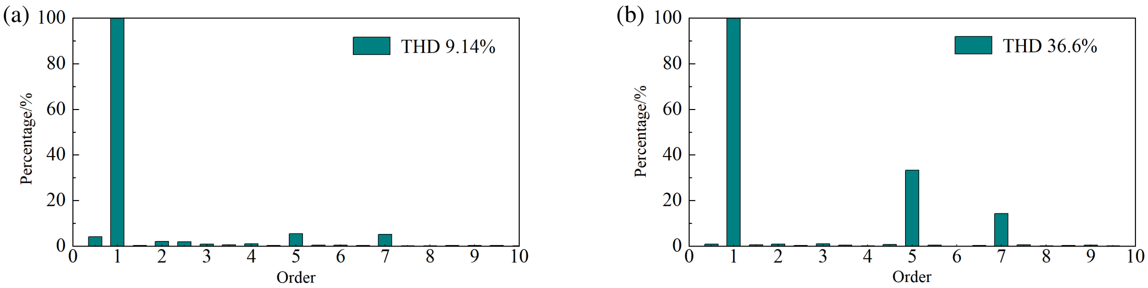

FIGURE 12. Comparison of current harmonic contents. (a) Fault-tolerant method with harmonic suppression. (b) Conventional fault-tolerant method.

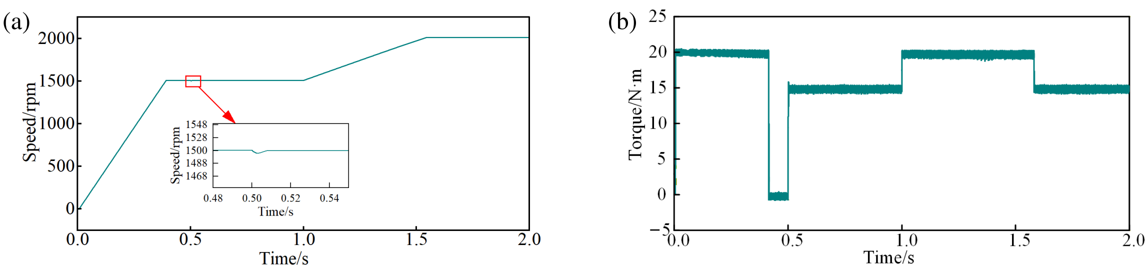

FIGURE 13. Operating result waveforms under different conditions. (a) Speed waveform. (b) Torque waveform.

nusoidal characteristics are largely retained, thereby enabling fault-tolerant operation. In contrast, as shown in Fig. 10(c), when the non-harmonic-suppression direct torque fault-tolerant control method is applied, significant fifth- and seventh-order harmonic components are introduced due to the inherent characteristics of the dual three-phase motor. As a result, the current waveform deviates from sinusoidal form, making stable motor operation difficult to ensure.

The current harmonic distributions under the harmonic-suppression fault-tolerant method and the conventional fault-tolerant method are compared in Fig. 12. In Fig. 12(a), the 5th and 7th harmonic components are relatively small, and the total harmonic distortion (THD) is only 9.14%. In contrast, in Fig. 12(b), the amplitudes of the 5th and 7th harmonics are significantly increased, resulting in a THD as high as 36.6%. This indicates that the latter method is insufficient in suppressing higher-order harmonics, which may lead to additional losses, increased noise, and aggravated electromagnetic interference. Therefore, the method corresponding to Fig. 12(a) is considered more advantageous in improving current quality and enhancing system stability.

The stability verification results of the fault-tolerant control method under different operating conditions are illustrated in Fig. 13. During 0–0.4 s, the motor was started under no-load conditions, and the speed was linearly increased to approximately 1500 rpm and then maintained at a stable level, while the torque was sustained at about $20\,\mathrm{N \cdot m}$. After the acceleration was completed, the motor entered the steady no-load operation stage, where the torque was kept at a low level to maintain no-load running. At 0.5 s, a load torque of $15\,\mathrm{N \cdot m}$ was applied, upon which the motor torque was rapidly elevated to the corresponding value, and the speed exhibited a slight fluctuation before quickly recovering to 1500 rpm, demonstrating a favorable dynamic response of the fault-tolerant control strategy. At 1.0 s, the reference speed was increased from 1500 rpm to 2000 rpm, and the torque responded synchronously by rising to approximately $20\,\mathrm{N \cdot m}$, thereby verifying the stability of the system during loaded acceleration. After the acceleration was completed at 1.6 s, the speed was stabilized at 2000 rpm, and the torque eventually settled at about $15\,\mathrm{N \cdot m}$. The overall waveforms indicate that the proposed fault-tolerant control method possesses satisfactory load response and regulation capability under various operating conditions.

6. CONCLUSION

A fault-tolerant control strategy based on a five-leg inverter topology was proposed for dual three-phase synchronous reluctance motors under single-phase open-circuit faults. By enabling bridge-arm sharing between the faulty and healthy phases, most of the critical space voltage vectors are preserved, and the missing vectors are effectively compensated through vector synthesis. As a result, the machine maintains an approximately circular flux linkage trajectory and a stable torque output even after a fault occurs.

Simulation results demonstrate that the proposed strategy not only significantly suppresses the 5th and 7th harmonic components and reduces the torque ripple but also partially preserves the pre-fault performance. Consequently, the overall system reliability and fault-tolerance capability were substantially improved. This study provides a new technical approach for the fault-tolerant control of multiphase machines and shows strong potential for engineering applications and practical deployment.

ACKNOWLEDGEMENT

This work was supported by State Grid Henan Electric Power Company Science and Technology Project (521790250002).

REFERENCES

[1] Jiang, Q., Y. Liu, Y. Yan, Q. Liu, S. Chen, and X. Jiang, "Substation inspection robot PTZ camera alignment method for high zoom scenes," *Proceedings of the CSEE*, Vol. 44, No. 8, 3337–3347, 2024.

[2] Yang, Z., Q. Fang, Z. Zhang, X. Liu, X. Xu, Y. Yan, and C. Miao, "Research on optimal control strategy for unpowered downslope of high-voltage inspection robot based on motor temperature rise in complexity microgrid networks," *Complexity*, Vol. 2021, No. 1, 6659941, 2021.

[3] Hou, J., B. Zhang, X. Liu, G. Huang, D. Xue, X. Wen, and X. Jiang, "Charging system design and charging strategy of overhead trans-mission line inspection robot on tower," *Science Technology and Engineering*, Vol. 22, No. 28, 12 388–12 394, 2022.

[4] Suzuki, H., K. Hirata, N. Niguchi, and K. Takahara, "Fault-tolerant control for a six-phase two-controllable-rotor motor," *IEEE Transactions on Magnetics*, Vol. 59, No. 4, 1–7, 2023.

[5] Herrera, D., J. Villegas, E. Galván, and J. M. Carrasco, "Powertrain EV synchronous reluctance motor design with redundant topology with novel control," *IET Electric Power Applications*, Vol. 13, No. 11, 1647–1659, 2019.

[6] Kamel, T., P. Amor, N. Polater, Y. Zhang, Z. Tian, S. Hillmansen, and P. Tricoli, "Development of a smart hybrid drive system with advanced logistics for railway applications," *International Journal of Hydrogen Energy*, Vol. 52, 559–576, 2024.

[7] Huang, S., L. Zhao, J. Zheng, and Y. Zhao, "Space vector pulse width modulation strategy for six-phase voltage source inverter in full modulation range based on sector subdivision method," *Transactions of China Electrotechnical Society*, Vol. 34, No. 24, 5070–5083, 2019.

[8] Mai, Z., F. Xiao, J. Liu, W. Zhang, and C. Lian, "Harmonic current suppression strategy of dual three-phase permanent magnet synchronous motor based on quasi proportional resonant cascading PI," *Transactions of China Electrotechnical Society*, Vol. 33, No. 24, 5751–5759, 2018.

[9] Zhang, J., K. Wang, S. Zhu, and D. Liu, "Control strategies of dual three-phase permanent magnet machines with multi-harmonics," *Proceedings of the CSEE*, Vol. 40, No. 2, 644–651, 2020.

[10] Shao, B., Z.-Q. Zhu, J. H. Feng, S. Y. Guo, Y. F. Li, L. Feng, and B. Shuang, "Improved direct torque control method for dual-three-phase permanent-magnet synchronous machines with back EMF harmonics," *IEEE Transactions on Industrial Electronics*, Vol. 68, No. 10, 9319–9333, 2021.

[11] Nandawadekar, A., M. R. Rashmi, and K. K. Nipin, "Lookup table based switching selection for direct torque controlled multiphase asynchronous machine drive," *Journal of the Institution of Engineers (India): Series B*, Vol. 103, No. 5, 1605–1618, 2022.

[12] Huang, L., J. Ji, W. Zhao, H. Tang, T. Tao, and S. Jin, "Direct torque control for dual three-phase permanent magnet motor with improved torque and flux," *IEEE Transactions on Energy Conversion*, Vol. 37, No. 4, 2385–2397, 2022.

[13] Wu, K., Y. Zhang, W. Lu, Y. Qi, and W. Shi, "Harmonic suppression in permanent magnet synchronous motor currents based on quasi-proportional-resonant sliding mode control," *Applied Sciences*, Vol. 14, No. 16, 7206, 2024.

[14] Xu, J., S. Guo, H. Guo, and X. Tian, "Fault-tolerant current control of six-phase permanent magnet motor with multifrequency quasi-proportional-resonant control and feedforward compensation for aerospace drives," *IEEE Transactions on Power Electronics*, Vol. 38, No. 1, 283–293, 2023.

[15] Wang, X., Z. Wang, M. Gu, Z. Xu, Z. Zou, W. Wang, and M. Cheng, "Fault-tolerant control of common electrical faults in dual three-phase PMSM drives fed by T-type three-level inverters," *IEEE Transactions on Industry Applications*, Vol. 57, No. 1, 481–491, 2021.

[16] Zhou, H., X. Xiang, H. Li, H. Zhang, S. He, and K. Li, "Magnetomotive force balance-based open-circuit fault diagnosis for T-type three-level inverter-fed dual three-phase PMSM drives," *IEEE Transactions on Power Electronics*, Vol. 41, No. 1, 966–982, 2026.

[17] Yang, J., T. Li, and G. Yang, "Modeling and control of dual three-phase PMSM with one open phase," *Transactions of China Electrotechnical Society*, Vol. 26, No. 10, 167–173, 2011.

[18] Li, W., P. Song, Q. Li, Z. Li, and N. C. Kar, "Open-phase fault modeling for dual three-phase PMSM using vector space decomposition and negative sequence components," *IEEE Transactions on Magnetics*, Vol. 58, No. 8, 1–6, 2022.

[19] Zheng, B., B. Li, Y. Xu, J. Zou, G. Yu, and M. Zhao, "Modeling and fault-tolerant control for DTP-PMSM with one phase open circuit fault considering voltage constraints," *Proceedings of the CSEE*, Vol. 43, No. 1, 294–303, 2023.

[20] Zhao, L., B. Ge, H. Gao, and D. Tao, "Fault-tolerant control for reducing harmonic distortion of dual three-phase permanent magnet synchronous motor," *Energies*, Vol. 15, No. 11, 3887, 2022.

[21] Wang, X., Z. Wang, M. He, Q. Zhou, X. Liu, and X. Meng, "Fault-tolerant control of dual three-phase PMSM drives with minimized copper loss," *IEEE Transactions on Power Electronics*, Vol. 36, No. 11, 12 938–12 953, 2021.

[22] Ai, X., L. Xiao, and Q. Wu, "Fault-tolerant control strategy of open-phase fault with minimum loss in full torque operation range for DTP-PMSM based on harmonic current injection," *Transactions of China Electrotechnical Society*, Vol. 40, No. 10, 3157–3169, 2025.

[23] Geng, Q., Z. Qin, X. Jin, G. Zhang, and Z. Zhou, "Direct torque control of dual three-phase permanent magnet synchronous motors based on master-slave virtual vectors," *World Electric Vehicle Journal*, Vol. 15, No. 5, 199, 2024.

[24] Shao, B., Z. Q. Zhu, J. Feng, S. Guo, Y. Li, and W. Liao, "Compensation of selective current harmonics for switching-table-based direct torque control of dual three-phase PMSM drives," *IEEE Transactions on Industry Applications*, Vol. 57, No. 3, 2505–2515, 2021.

[25] Yan, X., S. Ai, C. Li, and D. Mei, "Fault-tolerant control of dual three-phase PMSM based on minimum copper loss under multi-phase open and open-switch faults," *Journal of Electrical Engineering & Technology*, Vol. 19, No. 5, 3163–3174, 2024.